PHYSICAL REVIEW B **89**, 085131 (2014)

Time-dependent Landauer-Büttiker formula: Application to transient dynamics in graphene nanoribbons

Riku Tuovinen,[1] Enrico Perfetto,[2] Gianluca Stefanucci,[2,3,4] and Robert van Leeuwen[1,4]
[1]*Department of Physics, Nanoscience Center, FIN 40014, University of Jyväskylä, Finland*
[2]*Dipartimento di Fisica, Università di Roma Tor Vergata, Via della Ricerca Scientifica 1, I-00133 Rome, Italy*
[3]*Laboratori Nazionali di Frascati, Istituto Nazionale di Fisica Nucleare, Via E. Fermi 40, 00044 Frascati, Italy*
[4]*European Theoretical Spectroscopy Facility (ETSF)*
(Received 21 December 2013; published 27 February 2014)

In this work, we develop a time-dependent extension of the Landauer-Büttiker approach to study transient dynamics in time-dependent quantum transport through molecular junctions. A key feature of the approach is that it provides a closed integral expression for the time dependence of the density matrix of the molecular junction after switch-on of a bias in the leads or a perturbation in the junction, which in turn can be evaluated without the necessity of propagating individual single-particle orbitals or Green's functions. This allows for the study of time-dependent transport in large molecular systems coupled to wide-band leads. As an application of the formalism, we study the transient dynamics of zigzag and armchair graphene nanoribbons of different symmetries. We find that the transient times can exceed several hundreds of femtoseconds while displaying a long-time oscillatory motion related to multiple reflections of the density wave in the nanoribbons at the ribbon-lead interface. This temporal profile has a shape that scales with the length of the ribbons and is modulated by fast oscillations described by intraribbon and ribbon-lead transitions. Especially in the armchair nanoribbons there exists a sequence of quasistationary states related to reflections at the edge state located at the ribbon-lead interface. In the case of zigzag nanoribbons, there is a predominant oscillation frequency associated with virtual transitions between the edge states and the Fermi levels of the electrode. We further study the local bond currents in the nanoribbons and find that the parity of the edges strongly affects the path of the electrons in the nanoribbons. We finally study the behavior of the transients for various added potential profiles in the nanoribbons.

DOI: 10.1103/PhysRevB.89.085131　　PACS number(s): 73.63.−b, 73.23.Ad, 81.05.U−

I. INTRODUCTION

The Landauer-Büttiker (LB) formalism [1,2] has been a real milestone in the quantum theory of charge transport. Its success is attributable to the simplicity of the LB equations, which provide a transparent and physically intuitive picture of the steady-state current, as well as to the possibility of combining the formalism with density-functional theory (DFT) for first-principles calculations [3–9]. Nevertheless, due to the rising interest in the microscopic understanding of ultrafast charge-transfer mechanisms, the last decade has seen heightened effort in going beyond the (steady-state) LB formalism, thus accessing the transient regime. Different time-dependent (TD) approaches have been proposed to deal with different systems. Approaches based on the real-time propagation of scattering states [10–15], wave packets [16–18], extended states with sharp boundaries [19–22] or complex absorbing potentials [23–25], and noninteracting Green's functions [26–37] are suited to include the electron-electron interaction in a DFT framework. Interactions can alternatively be treated using nonequilibrium diagrammatic perturbation theory and solving the Kadanoff-Baym equations for open systems [38–40]. Several nonperturbative methods have been put forward too but, at present, they are difficult to use for first-principles calculations. These include master-equation-type approaches [41–47], real-time path-integral methods [48–51], nonequilibrium renormalization group methods [52–58], the quantum-trajectory approach [59,60], the TD density matrix renormalization group [61–65], and the nonequilibrium dynamical mean field theory [66,67].

In its original formulation, the LB formalism treats the electrons as noninteracting. Indubitably, the neglection of the electron-electron and electron-phonon interactions is in many cases a too crude approximation. However, in the ballistic regime, interaction effects play a minor role and the LB formalism is, still today, very useful to explain and fit several experimental curves. For instance, the identification of the different transport mechanisms, the temperature dependence of the current, the exponential decay of the conductance as a function of the length of the junction, etc., can all be interpreted within the LB formalism [68]. The TD approaches previously mentioned have the merit of extending the quantum transport theory to the time domain. However, they all are computationally more expensive and less transparent than the LB formalism *even for noninteracting electrons*. Therefore, considering the widespread use of the LB formalism in both the theoretical and experimental communities, it is natural to look for a TD-LB formula which could give the current at time t at the same computational cost as at the steady state.

For a single level initially isolated and then contacted to source and drain electrodes, a TD-LB formula was derived by Jauho *et al.* in 1994 [69]. The treatment of the contacts in the initial state introduces some complications which, however, were overcome about 10 years later [70]. The approach of Ref. [70] was then applied to generalize the TD-LB formula to a single level with spin [71]. Nevertheless, only recently we have been able to derive a TD-LB formula for arbitrary scattering regions [72,73]. The only restriction of this formula is that the density of states of the source and drain electrodes is smooth and wide enough that the wide-band limit approximation (WBLA) applies. In this case, one can derive a TD-LB formula not only for the total current, but for the full one-particle density matrix. The explicit analytic result allows for interpretation of typical transient oscillations in terms of electronic transitions within the molecular junction or between the junction and the leads, as well as the different damping times. Owing to the low computational cost, one can consider very large systems and arbitrarily long propagation times.

In this work, we briefly review the results of Refs. [72,73] and generalize them to include arbitrary perturbations in the molecular junction. We further present a convenient implementation scheme to extract densities and local currents, and demonstrate the feasibility of the method in graphene nanoribbons (GNR) [74–77]. So far, real-time investigations of GNRs have been limited to small size [78] and weak biases [79]. As the TD-LB formalism is not limited to weak driving fields we could study the transient dynamics in the unexplored strong-bias regime. In GNRs there are plenty of interesting nanoscale size effects depending on the topology of the edges. Our main findings are that for large biases (i) the time to relax to the steady state exceeds hundreds of femtoseconds; (ii) in the transient current and density of zigzag GNRs there is a predominant oscillation frequency associated with virtual transitions between the edge states and the Fermi levels of the electrodes; (iii) the currents in the armchair GNRs exhibit a sequence of quasistationary states whose duration increases with the length of the GNR; and (iv) the parity of the edges strongly affects the path of the electrons inside the GNR.

The paper is organized as follows. In Sec. II, we introduce the system and present the main results of the TD-LB formalism. Here, we also illustrate the implementation scheme and defer the numerical details to the Appendix. The TD results on GNRs are collected in Sec. III where we investigate the effects of the edge states, the quasistationary currents, the even-odd parity effect on the current-density profile, and a perturbed GNR. Finally, we draw our conclusions in Sec. IV.

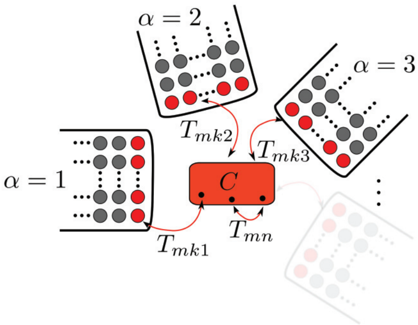

FIG. 1. (Color online) Schematic of the quantum transport setup: a noninteracting central region C is coupled to an arbitrary number of leads.

II. THEORETICAL BACKGROUND

A. System setup and earlier work

We investigate quantum transport between metallic wide-band leads and a noninteracting central region. The setup is otherwise as general as possible; the number and the structure of the leads are arbitrary as is the size and the structure of the central region. The Hamiltonian is of the form

$$\hat{H} = \sum_{k\alpha,\sigma} \epsilon_{k\alpha} \hat{d}^\dagger_{k\alpha,\sigma}\hat{d}_{k\alpha,\sigma} + \sum_{mn,\sigma} T_{mn}\hat{d}^\dagger_{m,\sigma}\hat{d}_{n,\sigma} + \sum_{mk\alpha,\sigma}\left(T_{mk\alpha}\hat{d}^\dagger_{m,\sigma}\hat{d}_{k\alpha,\sigma} + T_{k\alpha m}\hat{d}^\dagger_{k\alpha,\sigma}\hat{d}_{m,\sigma}\right). \tag{1}$$

Here, σ is a spin index and $k\alpha$ denotes the kth basis function of the αth lead while m and n label basis states in the central region. The corresponding creation and annihilation operators for these states are denoted by $\hat{d}^\dagger$ and $\hat{d}$, respectively. The single-particle levels of the leads are given by $\epsilon_{k\alpha}$ while the matrices T give the hoppings between the molecular and molecule-lead states. This is depicted schematically in Fig. 1.

At times $t < t_0$, the system is in thermal equilibrium at inverse temperature β and chemical potential μ, the density matrix having the form $\hat{\rho} = \frac{1}{\mathcal{Z}} e^{-\beta(\hat{H}-\mu\hat{N})}$ where $\mathcal{Z}$ is the grand-canonical partition function of the connected lead-molecule system. At $t = t_0$, a sudden bias of the form

$$\hat{V} = \theta(t - t_0) \sum_{k\alpha,\sigma} V_\alpha \hat{d}^\dagger_{k\alpha,\sigma}\hat{d}_{k\alpha,\sigma}$$

is applied to leads, where V_α is the bias strength in lead α. This potential drives the system out of equilibrium and charge carriers start to flow through the central region. To calculate the time-dependent current, we use the equations of motion for the one-particle Green's function on the Keldysh contour $\gamma_{\rm K}$. This quantity is defined as the ensemble average of the contour-ordered product of particle creation and annihilation operators in the Heisenberg picture [72]

$$G_{rs}(z,z') = -i\langle \mathcal{T}_{\gamma_{\rm K}}[\hat{d}_{r,{\rm H}}(z)\hat{d}^\dagger_{s,{\rm H}}(z')]\rangle, \tag{2}$$

where the indices r, s can be either indices in the leads or in the central region and the variables z, z' run on the contour. This contour has a forward and a backward branch on the real-time axis $[t_0,\infty[$ and also a vertical branch on the imaginary axis $[t_0, t_0 - i\beta]$ describing the initial preparation of the system [39]. The matrix $\boldsymbol{G}$ with matrix elements G_{rs} satisfies the equations of motion [80]

$$\left[i\frac{d}{dz} - \boldsymbol{h}(z)\right]\boldsymbol{G}(z,z') = \delta(z,z')\mathbf{1}, \tag{3}$$

$$\boldsymbol{G}(z,z')\left[-i\frac{\overleftarrow{d}}{dz'} - \boldsymbol{h}(z')\right] = \delta(z,z')\mathbf{1}, \tag{4}$$

with Kubo-Martin-Schwinger boundary conditions, i.e., the Green's function is antiperiodic along the contour. Here, $\boldsymbol{h}(z)$ is the single-particle Hamiltonian. In the basis $k\alpha$ and m the matrix $\boldsymbol{h}$ has the following block structure:

$$\boldsymbol{h} = \begin{pmatrix} h_{11} & 0 & 0 & \dots & h_{1C} \\ 0 & h_{22} & 0 & \dots & h_{2C} \\ 0 & 0 & h_{33} & \dots & h_{3C} \\ \vdots & \vdots & \vdots & \ddots & \vdots \\ h_{C1} & h_{C2} & h_{C3} & \dots & h_{CC} \end{pmatrix}, \tag{5}$$

where $(h_{\alpha\alpha'})_{kk'} = \delta_{\alpha\alpha'}\delta_{kk'}\epsilon_{k\alpha}$ corresponds to the leads, $(h_{\alpha C})_{km} = T_{k\alpha m}$ is the coupling part, and $(h_{CC})_{mn} = T_{mn}$ accounts for the central region. We approximate the retarded embedding self-energy as a purely imaginary constant, according to WBLA:

$$\Sigma^{\mathrm{R}}_{\alpha,mn}(\omega) = \sum_k T_{mk\alpha}\frac{1}{\omega - \epsilon_{k\alpha} - V_\alpha + i\eta}T_{k\alpha n} = -\frac{i}{2}\Gamma_{\alpha,mn}. \tag{6}$$

In other words, the level-width functions Γ_α appear as the wide-band approximation for the retarded embedding self-energy $\Sigma^{\mathrm{R}}_\alpha(\omega) = -i\Gamma_\alpha/2$ for which $\Gamma = \Sigma_\alpha\Gamma_\alpha$. Due to the coupling between the central region and the leads, the matrix $\boldsymbol{G}$ has nonvanishing entries everywhere:

$$\boldsymbol{G} = \begin{pmatrix} G_{11} & \dots & G_{1C} \\ \vdots & \ddots & \vdots \\ G_{C1} & \dots & G_{CC} \end{pmatrix}. \tag{7}$$

The equations of motion (3) and (4) for the Green's function G_{CC} projected onto the central region have been solved analytically in WBLA [73] to give the time-dependent one-particle reduced density matrix (TD1RDM) as the equal-time limit $\rho(t) = -iG^<_{CC}(t,t)$:

$$\begin{aligned}\rho(t) = \int\frac{d\omega}{2\pi}f(\omega-\mu)\sum_\alpha\big\{&A_\alpha(\omega+V_\alpha)\\ &+V_\alpha[e^{i(\omega+V_\alpha-h_{\mathrm{eff}})t}G^{\mathrm{R}}(\omega)A_\alpha(\omega+V_\alpha)+\mathrm{H.c.}]\\ &+V_\alpha^2 e^{-ih_{\mathrm{eff}}t}G^{\mathrm{R}}(\omega)A_\alpha(\omega+V_\alpha)G^{\mathrm{A}}(\omega)e^{ih^\dagger_{\mathrm{eff}}t}\big\},\end{aligned} \tag{8}$$

where f is the Fermi function, $G^{\mathrm{R}}(\omega) = (\omega - h_{\mathrm{eff}})^{-1}$ and $G^{\mathrm{A}}(\omega) = [G^{\mathrm{R}}(\omega)]^\dagger$ are the retarded and advanced Green's functions, $h_{\mathrm{eff}} = h_{CC} - i\Gamma/2$ is the effective single-particle Hamiltonian, and the partial spectral functions are $A_\alpha(\omega) = G^{\mathrm{R}}(\omega)\Gamma_\alpha G^{\mathrm{A}}(\omega)$. The full spectral function is then simply $A(\omega) = \Sigma_\alpha A_\alpha(\omega)$.

We emphasize that Eq. (8) is an explicit closed formula for the equal time $G^<$ or, equivalently, for the TD1RDM. All the quantities inside the integral can be calculated without the need of storing auxiliary quantities at earlier times. In other words, if we want to know the TD1RDM at time t, we simply need to evaluate the integral in Eq. (8). As no propagation is required, we have access to nonequilibrium quantities at arbitrary times after the switch-on of the bias. This is the most important feature of Eq. (8). In fact, for large and weakly coupled junctions, the transient regime can exceed several hundreds of femtoseconds and, at present, these time scales are out of reach of the available TD approaches.

Similarly to the TD1RDM, the time-dependent current through the interface of the αth lead has an explicit closed expression which generalizes the LB formula to the time domain [73]

$$\begin{aligned}I_\alpha(t) = -2\int\frac{d\omega}{2\pi}f(\omega-\mu)\sum_\beta \mathrm{Tr}\big\{&\Gamma_\alpha G^{\mathrm{R}}(\omega+V_\beta)\Gamma_\beta G^{\mathrm{A}}(\omega+V_\beta) - \Gamma_\alpha G^{\mathrm{R}}(\omega+V_\alpha)\Gamma_\beta G^{\mathrm{A}}(\omega+V_\alpha)\\ &+V_\beta[\Gamma_\alpha e^{i(\omega+V_\beta-h_{\mathrm{eff}})t}G^{\mathrm{R}}(\omega)(-i\delta_{\alpha\beta}G^{\mathrm{R}}(\omega+V_\beta)+A_\beta(\omega+V_\beta))+\mathrm{H.c.}]\\ &+V_\beta^2\Gamma_\alpha e^{-ih_{\mathrm{eff}}t}G^{\mathrm{R}}(\omega)A_\beta(\omega+V_\beta)G^{\mathrm{A}}(\omega)e^{ih^\dagger_{\mathrm{eff}}t}\big\},\end{aligned} \tag{9}$$

where β runs over all the leads. As h_{eff} is non-Hermitian, the terms in the last two rows of Eq. (9) vanish exponentially when $t \to \infty$ and one recovers the steady-state LB formula. It is easy to verify that the current correctly vanishes for all t at zero bias, $V_\alpha = 0$, and for $t = 0$ at any bias. In the remainder of this section, we present a convenient numerical procedure to evaluate Eq. (8) as well as a generalization of the same formula to include arbitrary spatially dependent perturbations in the central region.

B. Expansion in the h_{eff} eigenbasis

We expand the result in Eq. (8) in the eigenbasis of the non-Hermitian effective Hamiltonian h_{eff}. This object has separate left and right eigenvectors forming a mutually *biorthogonal* set $\{|\Psi^{\mathrm{L}}_j\rangle, |\Psi^{\mathrm{R}}_j\rangle\}$ with

$$\langle\Psi^{\mathrm{L}}_j|h_{\mathrm{eff}} = \epsilon_j\langle\Psi^{\mathrm{L}}_j|, \quad h_{\mathrm{eff}}|\Psi^{\mathrm{R}}_j\rangle = \epsilon_j|\Psi^{\mathrm{R}}_j\rangle. \tag{10}$$

By the biorthogonality we have $\langle\Psi^{\mathrm{L}}_j|\Psi^{\mathrm{R}}_k\rangle = \delta_{jk}\langle\Psi^{\mathrm{L}}_j|\Psi^{\mathrm{R}}_j\rangle$, where we can choose an appropriate normalization of the diagonal elements.

We notice that in Eq. (8), in every term there is h_{eff} on the left and $h^\dagger_{\mathrm{eff}}$ on the right. This in mind, and looking at how the matrix operates in Eq. (10), we choose to expand in the "left-left" eigenbasis, i.e., we multiply the density matrix in Eq. (8) from left with a row vector $\langle\Psi^{\mathrm{L}}|$ and from the right by a column vector $|\Psi^{\mathrm{L}}\rangle$. In order to calculate a matrix element $\langle m|\rho(t)|n\rangle$ in the original basis of region C, we insert a complete set of left and right eigenvectors of h_{eff}. The resolution of identity reads as

$$\mathbf{1} = \sum_j\frac{|\Psi^{\mathrm{R}}_j\rangle\langle\Psi^{\mathrm{L}}_j|}{\langle\Psi^{\mathrm{L}}_j|\Psi^{\mathrm{R}}_j\rangle} = \sum_j\frac{|\Psi^{\mathrm{L}}_j\rangle\langle\Psi^{\mathrm{R}}_j|}{\langle\Psi^{\mathrm{R}}_j|\Psi^{\mathrm{L}}_j\rangle} \tag{11}$$

and hence

$$\langle m|\rho(t)|n\rangle = \sum_{j,k}\frac{\langle m|\Psi^{\mathrm{R}}_j\rangle}{\langle\Psi^{\mathrm{L}}_j|\Psi^{\mathrm{R}}_j\rangle}\frac{\langle\Psi^{\mathrm{R}}_j|n\rangle}{\langle\Psi^{\mathrm{R}}_k|\Psi^{\mathrm{L}}_k\rangle}\langle\Psi^{\mathrm{L}}_j|\rho(t)|\Psi^{\mathrm{L}}_k\rangle. \tag{12}$$

The matrix elements $\rho_{jk}(t) = \langle \Psi_j^{\mathrm{L}} | \rho(t) | \Psi_k^{\mathrm{L}} \rangle$ can easily be extracted from Eq. (8) and read as

$$\begin{aligned}\rho_{jk}(t) = {}& \sum_{\alpha} \mathit{\Gamma}_{\alpha,jk} \mathit{\Lambda}_{\alpha,jk} \\ &+ \sum_{\alpha} V_\alpha \mathit{\Gamma}_{\alpha,jk} [\mathit{\Pi}_{\alpha,jk}(t) + \mathit{\Pi}^*_{\alpha,kj}(t)] \\ &+ \sum_{\alpha} V_\alpha^2 \mathit{\Gamma}_{\alpha,jk} e^{-i(\epsilon_j - \epsilon_k^*)t} \mathit{\Omega}_{\alpha,jk}\end{aligned} \tag{13}$$

with

$$\mathit{\Gamma}_{\alpha,jk} = \langle \Psi_j^{\mathrm{L}} | \mathit{\Gamma}_\alpha | \Psi_k^{\mathrm{L}} \rangle \tag{14}$$

and

$$\mathit{\Lambda}_{\alpha,jk} = \int \frac{d\omega}{2\pi} \frac{f(\omega-\mu)}{(\omega + V_\alpha - \epsilon_j)(\omega + V_\alpha - \epsilon_k^*)}\ , \tag{15}$$

$$\mathit{\Pi}_{\alpha,jk}(t) = \int \frac{d\omega}{2\pi} \frac{f(\omega-\mu) e^{i(\omega + V_\alpha - \epsilon_j)t}}{(\omega - \epsilon_j)(\omega + V_\alpha - \epsilon_j)(\omega + V_\alpha - \epsilon_k^*)}, \tag{16}$$

$$\begin{aligned}&\mathit{\Omega}_{\alpha,jk} \\ &\quad = \int \frac{d\omega}{2\pi} \frac{f(\omega-\mu)}{(\omega - \epsilon_j)(\omega + V_\alpha - \epsilon_j)(\omega + V_\alpha - \epsilon_k^*)(\omega - \epsilon_k^*)}.\end{aligned} \tag{17}$$

The first row of Eq. (13) gives the steady-state value of the TD1RDM. The time-dependent part is contained in the functions $\mathit{\Pi}$ in the second row and in the exponential in the third row. By inspection of Eq. (13) we see that transitions between the leads and the central region are described by the terms $\mathit{\Pi}$ (oscillations of frequency $\omega_j = |V_\alpha - \mathrm{Re}\,\epsilon_j|$), whereas transitions within the central region are described by the exponential term in the third line (oscillations of frequency $\omega_{jk} = |\mathrm{Re}\,\epsilon_j - \mathrm{Re}\,\epsilon_k|$) [73]. As the eigenvalues ϵ_j are, in general, complex, we infer that electronic transitions between states in the central region are damped faster than those involving states at the Fermi energies $\mu + V_\alpha$. In the zero-temperature limit, the integrals in Eqs. (15)–(17) are given in terms of logarithms and exponential integral functions (of complex variable), which can be evaluated using an extremely accurate numerical algorithm proposed recently in the context of computer graphics [81] (see Appendix A).

C. Switching-on of electric and magnetic fields in the central region

The TD1RDM of Eq. (8) and the TD current of Eq. (9) refer to systems driven out of equilibrium by an external bias. Here, we generalize these results to include the sudden switch-on of electric and/or magnetic fields in the central region. We consider the system described in Sec. II A with central-region Hamiltonian h_{CC} in equilibrium and $\widetilde{h}_{CC}$ for $t > t_0$, where t_0 is the time at which the bias is switched on. The switch-on of an electric field is useful to study, e.g., the effects of a gate voltage or to model the self-consistent voltage profile within the central region. In this case,

$$(\widetilde{h}_{CC})_{mn} = T_{mn} + u_{mn}, \tag{18}$$

where u_{mn} are the matrix elements of the scalar potential between two basis states of the central region. The switch-on of a magnetic field is instead useful to study, e.g., the Aharonov-Bohm effect in ring geometries or the Landau levels in planar junctions such as graphene nanoribbons. In this case,

$$(\widetilde{h}_{CC})_{mn} = T_{mn} e^{i\alpha_{mn}}, \tag{19}$$

where the sum of the Peierls phases $\alpha_{mn} = -\alpha_{nm}$ along a closed loop yields the magnetic flux (normalized to the flux quantum $\phi_0 = h/2e$) across the loop.

Having two different Hamiltonians for the central region (h_{CC} at times $t < t_0$ and $\widetilde{h}_{CC}$ at times $t > t_0$), we need to adjust the derivation worked out in the earlier study in Ref. [73]. By definition, the Matsubara Green's function remains unchanged since it only depends on the Hamiltonian at times $t < t_0$. On the other hand, for Green's functions having components on the horizontal branches of the Keldysh contour, we have to use the Hamiltonian $\widetilde{h}_{CC}$. The calculations are rather lengthy but similar to those presented in Ref. [73]; we outline the main steps in Appendix B and state here only the final result for the TD1RDM:

$$\begin{aligned}\rho(t) = \int \frac{d\omega}{2\pi} f(\omega-\mu) \sum_\alpha \{ & \widetilde{A}_\alpha(\omega + V_\alpha) \\ & + [e^{i(\omega + V_\alpha - \widetilde{h}_{\mathrm{eff}})t} G^{\mathrm{R}}(\omega) \widetilde{V}_\alpha \widetilde{A}_\alpha(\omega + V_\alpha) + \mathrm{H.c.}] \\ & + e^{-i\widetilde{h}_{\mathrm{eff}} t} G^{\mathrm{R}}(\omega) \widetilde{V}_\alpha \widetilde{A}_\alpha(\omega + V_\alpha) \widetilde{V}_\alpha^\dagger G^{\mathrm{A}}(\omega) e^{i\widetilde{h}_{\mathrm{eff}}^\dagger t} \},\end{aligned} \tag{20}$$

where the functions with a *tilde* signify that they are calculated using $\widetilde{h}_{CC}$, except for $\widetilde{V}_\alpha = V_\alpha \mathbf{1} - (\widetilde{h}_{CC} - h_{CC})$ which is to be understood as a matrix in this case [in Eq. (8) it was proportional to the identity matrix]. The retarded/advanced Green's functions in Eq. (20) do not have tilde since they originate from the analytic continuation of G^{M}. In the limit $\widetilde{h}_{CC} \to h_{CC}$, it is easy to check that the results in Eqs. (8) and (20) agree.

For the case of perturbed central region, we would also like to have a similar result as in Eq. (13). Since h_{eff} and $\widetilde{h}_{\mathrm{eff}}$ do not necessarily commute, the left/right eigenstates are not the same. For instance, in the second row of Eq. (20) we need to insert a complete set of left/right eigenstates of h_{eff} (resolution of the identity) in-between the first exponential and G^{R}, and so on. This leads to extra sums and overlaps between different bases. The resulting generalization of Eq. (13) is derived in Appendix B.

D. Physical content of the TD1RDM

From the TD1RDM in the left-left basis we can extract the matrix elements in the site basis according to Eq. (12). In the site basis, the diagonal elements give the site densities (or local occupations) of the central region. The off-diagonal elements are instead related to the bond currents and the kinetic energy density [14,82]. The site densities and the bond currents are related by the continuity equation $\partial_t n_m = \Sigma_n I_{mn}$, stating that the currents flowing in and out of site m must add up to the temporal change of density in that site. It is easy to show that the bond currents are given by

$$I_{mn} = 2\ \mathrm{Im}[T_{mn} e^{i\alpha_{mn}} \rho_{nm}]. \tag{21}$$

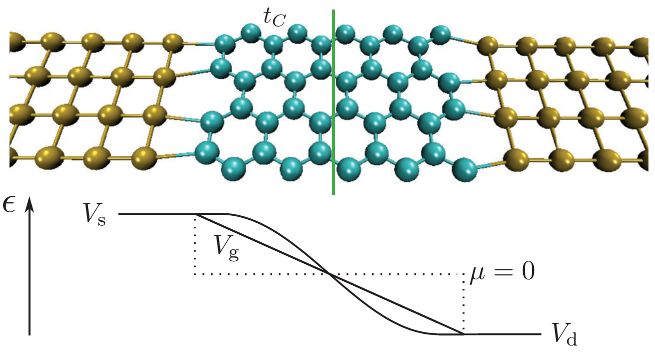

FIG. 2. (Color online) Transport setup of a (zigzag) graphene nanoribbon connected to metallic leads: contacts to leads are between doubly colored bonds; bridge (explained in text) is shown by the green cutting line. The structure of the leads is shown for illustrative purposes. Voltage profile is shown below the structure.

At the steady state ($t \to \infty$) one can verify that our equations for the TD1RDM correctly imply $\Sigma_n I_{mn} = 0$.

III. RESULTS

We implement the framework described in the previous section and in the Appendices to study the transient dynamics of GNRs coupled to metallic leads in the zero-temperature limit. We are especially interested to investigate the so-far unexplored region of large biases, where the Dirac (low-energy) Hamiltonian is inadequate. By looking at time-dependent quantities, such as densities and bond currents, we perform a sort of *spectroscopical* analysis by discrete Fourier transforming the transient curves and reveal the dominant transitions responsible for the slow relaxation to a steady state.

The transport setup is shown in Fig. 2. The leads are semi-infinite with terminal sites coupled to a GNR. The GNR is modeled by a single-orbital π-electron network, parametrized by nearest-neighbor hopping $t_C = -2.7$ eV [83]; second and third nearest-neighbor hoppings [83] are neglected but can be included at the same computational price. The size and the orientation [zigzag (zGNR), armchair (aGNR)] of the GNR can be chosen freely as well as the structure of the leads. The strength of the level-width functions $\varGamma_\alpha$ depends on both the couplings to the leads and the internal properties of the leads. Even though in our framework $\varGamma_\alpha$ can be any positive-semidefinite matrix [84,85], here we take it of the form

$$\varGamma_{\alpha,mn} = \gamma_\alpha \, \Delta_{\alpha,mn}, \tag{22}$$

where $\Delta_{\alpha,mn} = \delta_{mn}$ when m,n labels edge atoms contacted to lead α and $\Delta_{mn,\alpha} = 0$ otherwise. In our calculations, we choose $\gamma_\alpha = 0.1$ eV independent of α. The chemical potential is set to $\mu = 0$ in order to have a charge-neutral GNR in equilibrium. The system is driven out of equilibrium by a sudden symmetric bias voltage between source and drain electrodes, i.e., $V_\alpha = \pm V_{\rm sd}/2$. The strength of the potential profile within the central region is of amplitude $V_{\rm g}$ and can be, e.g., linear or sinusoidal as illustrated in Fig. 2, or of any other shape. To analyze the output of the numerical simulations, we consider a cutting line or a *bridge* in the middle of the GNR and calculate the sum of all bond currents for the bonds cut by the bridge (see Fig. 2). In the following, this sum of bond currents is denoted by I. We measure energies in units of $\epsilon = 1$ eV and therefore the unit of time $t = \hbar/\epsilon \approx 6.58 \times 10^{-16}$ s and the unit of current $I = e\epsilon/\hbar \approx 2.43 \times 10^{-4}$ A.

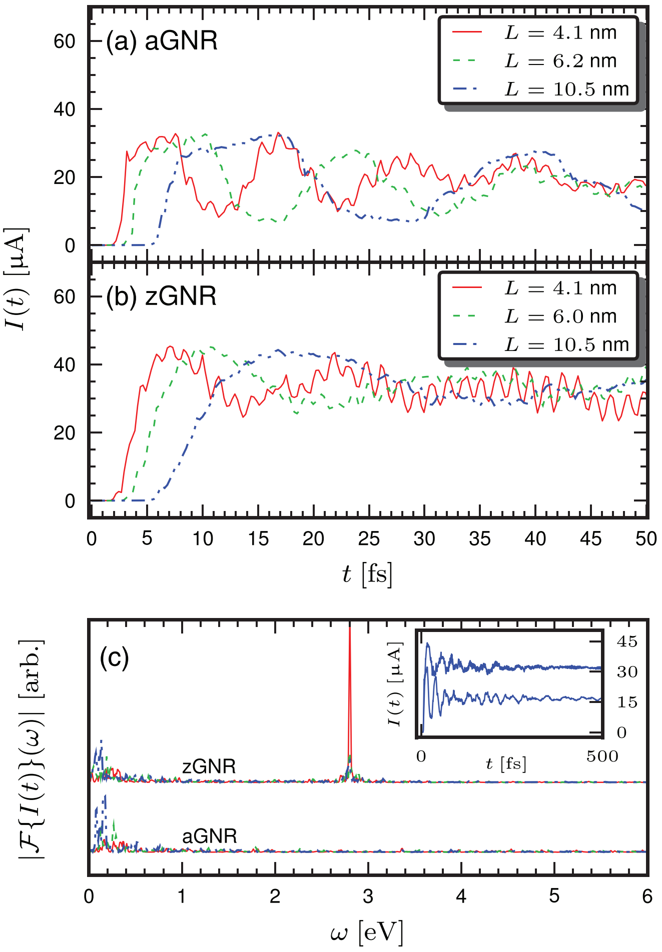

FIG. 3. (Color online) Time-dependent bond currents through ribbons of *varying length*: (a) aGNR [fixed width $W = 1.5$ nm (13)], (b) zGNR [fixed width $W = 1.6$ nm (8)], and (c) the corresponding Fourier transforms (zGNR is offset for clarity); the inset shows the long-time behavior of the currents for $L = 10.5$ nm in (a) and (b). [The line colors and styles correspond to those in (a) and (b).]

A. Transient spectroscopy of zGNR and aGNR

Let us study the dependence of the TD current on the length of the GNR at fixed width and bias voltage. For aGNRs of width 1.4 nm (this is a 13-aGNR where 13 refers to the number of armchair dimer rows [86]) and a zGNRs of width 1.6 nm (this is an 8-zGNR where 8 is the number of zigzag rows [86]), we show I in Figs. 3(a) and 3(b) and the Fourier transforms in Fig. 3(c). The Fourier transforms are calculated from the long-time simulations shown in the inset of Fig. 3(c) where we subtract the steady-state value from the sample points, take the absolute value of the result, and use Blackman-window filtering [87]. In both cases, the bias voltage is $V_{\rm sd} = 5.6$ eV and $V_{\rm g} = 0$ eV. By increasing the length of the ribbon, the initial transient starts with a delay since the current is measured

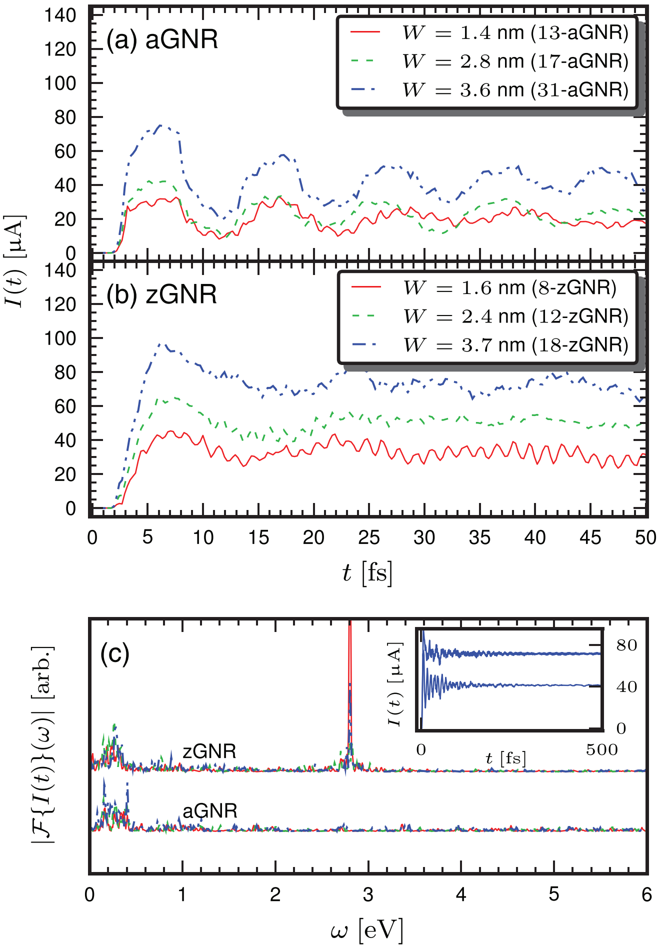

FIG. 4. (Color online) Time-dependent bond currents through ribbons of *varying width*: (a) aGNR (fixed length $L = 4.1$ nm), (b) zGNR (fixed length $L = 4.1$ nm), and (c) the corresponding Fourier transforms (zGNR is offset for clarity); the inset shows the long-time behavior of the currents for $W = 3.6$ nm in (a) and $W = 3.7$ nm in (b), respectively. [The line colors and styles correspond to those in (a) and (b).]

in the center (see Fig. 2), but the steady-state value is roughly the same. The overall number of states also increases, and hence more states close to the Fermi level are available as transport channels. Consequently, smaller transition energies become dominant and the peaks in the Fourier spectra shift towards smaller frequencies. For the zGNRs we also find a high-energy peak independent of the length; this peak is responsible for the fast superimposed oscillations in the time domain. The peak appears at frequency $\omega = V_{\mathrm{sd}}/2 = 2.8$ eV and therefore corresponds to transitions between the lead Fermi energy and zero-energy states in the ribbon, i.e., the edge states. The edge states are weakly coupled to the leads and therefore these transitions are slowly damped. As a matter of fact, similar high-frequency oscillations are visible in aGNRs as well [see Fig. 3(a)] . Nevertheless, the Fourier transform does not show any high-frequency peak in this case. In aGNRs, we have zigzag edges at the interface and hence edge states strongly coupled to the leads. The high-frequency oscillations in aGNRs are damped faster than in zGNRs [see the inset in Fig. 3(c)], and are not visible in the Fourier spectrum.

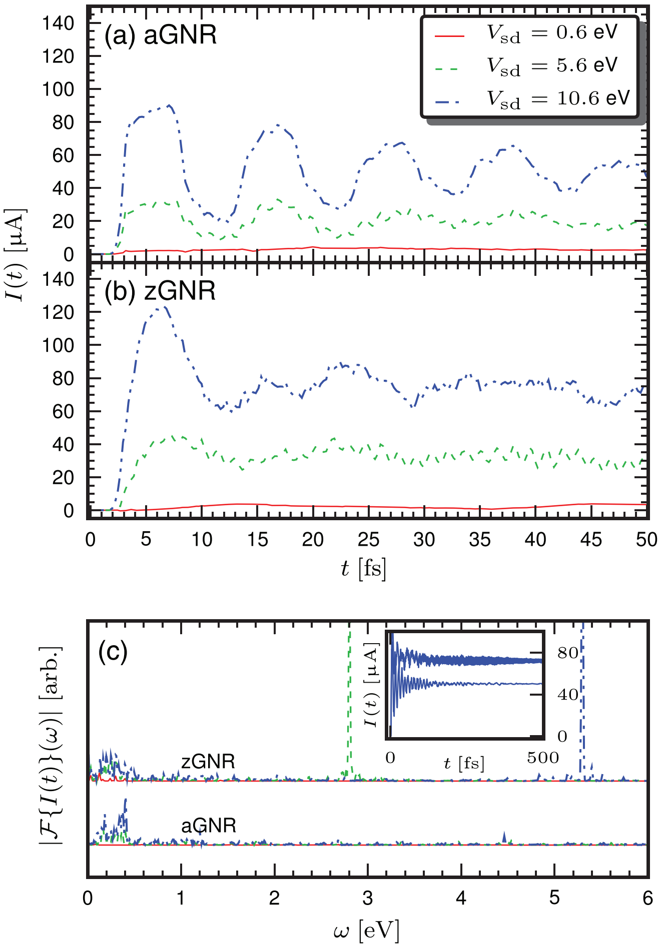

FIG. 5. (Color online) Time-dependent bond currents through fixed-size ribbons with *varying bias voltage* (a) aGNR [$W = 1.5$ nm (13), $L = 4.1$ nm], (b) zGNR [$W = 4.1$ nm (8), $L = 4.1$ nm], and (c) the corresponding Fourier transforms (zGNR is offset for clarity); the inset shows the long-time behavior of the currents for $V_{\mathrm{sd}} = 10.6$ eV in (a) and (b).

Next, we vary the width of the ribbons while keeping the length and the bias voltage fixed. In Fig. 4, we show the dependency on the width for aGNRs and zGNRs of length 4.1 nm. Depending on the width, the ribbon is either metallic or semiconducting [77]. However, as the gap in the semiconducting case is much smaller than the applied voltage $V_{\mathrm{sd}} = 5.6$ eV, the conducting properties are not affected by the gap. When increasing the width of the ribbon, the length of the bridge, through which the cumulative bond current I is calculated, increases and so does the steady-state value of I. However, the transient features remain the same as clearly illustrated in the Fourier spectrum of Fig. 4(c) . Thus, at difference with the results of Fig. 3(c), the widening of the ribbon does not cause a shift of the low-energy peaks toward smaller energies. As expected, this is true also for the high-energy peak in zGNRs, in agreement with the fact that the energy of the edge states is independent of the size of the ribbon.

As a third case, we study the effect of increasing the bias voltage (while still keeping $V_{\mathrm{g}} = 0$). In Figs. 5(a) and 5(c), we show the results for 13-aGNR of length 4.1 nm and width 1.4 nm, and in Figs. 5(b) and 5(c) the results for 8-zGNR of length 4.1 nm and width 1.6 nm (ribbons of comparable sizes). For zGNR, the frequency of the oscillations associated to the edge-state transitions increases linearly with the bias, as it should be. We also observe that for both ribbons the transient regime lasts longer the larger is the bias, and that the steady state is attained after several hundreds of femtoseconds.

As a general remark, of all the simulations shown in this section we can say that the absolute values of the steady-state currents are higher through zGNRs than through aGNRs (of comparable sizes). It is not easy to provide an intuitive explanation of this observation since at large biases there are very many states which contribute to the absolute value of the steady-state current. We also observe that the μA–mA range for the current with bias in the eV range agrees with the experimental results of Refs. [88–95].

B. Quasistationary currents

In Fig. 3(a), we notice the formation of quasistationary states as we increase the length of the ribbon. The current steeply increases from zero to some value and then grows linearly before decreasing again. The growth is slower and lasts longer the longer is the ribbon. Let us investigate further the dependence of the current on the length of the ribbon. In Fig. 6, we show the transient currents through 13-aGNR ($W = 1.4$ nm) and 8-zGNR ($W = 1.6$ nm) of similar lengths with $V_{\text{sd}} = 5.6$ eV. For graphical purposes, we normalize the current by the number of bonds in the bridge and the time by the length L of the ribbon. The curves do essentially collapse on one single curve. The peculiar feature of the aGNRs is the current plateau for $1 \lesssim t/L \lesssim 2$. The duration of the plateau corresponds to the time for an electron with velocity $v \sim 1$ nm/fs to cross the ribbon. This velocity is consistent with the value of the Fermi velocity $v_{\text{F}} = 3|t_C|a/(2\hbar)$ where $a = 1.42$ Å is the carbon-carbon distance [74]. The physical picture is that an almost steplike, right-moving density wave reaches the bridge (positioned in the middle of the ribbon) at $t/L \simeq \frac{1}{2}$ and the right interface at $t/L \simeq 1$. At this time, the wave is reflected backward and at time $t/L \simeq \frac{3}{2}$ reaches the bridge thus destroying the plateau. No pronounced plateau is instead observed in zGNRs. As we shall see in the next section, the current distribution along the ribbon is strongly dependent on the orientation of the bonds. The tilted bonds in zGNRs cause multiple reflections at the edges, thus preventing the formation of a current plateau. Also, more powerful reflection can be seen from the zigzag edge state (at the lead interface) in the case of aGNRs.

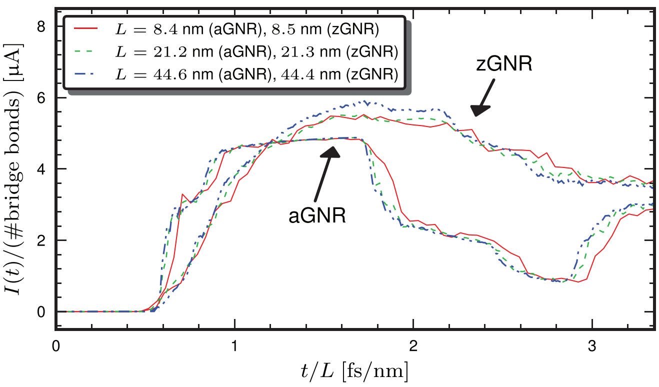

FIG. 6. (Color online) First transients of the time-dependent current through ribbons of varying length divided by the number of bonds in the bridge. The horizontal axis is scaled by the length of the corresponding ribbon.

C. Even-odd parity effects in charge and current profiles

The GNRs are parametrized by integer numbers (even or symmetric and odd or asymmetric) for width and length. In this section, we study how the parity of the GNRs affects the charge and current profiles in the transient regime. We choose ribbons of equivalent lengths, approximately 6 nm (14 armchair cells and 25 zigzag cells) and equivalent widths, approximately 1.5 nm. However, we take the widths as {7,8} zigzag lines and {12,13} armchair dimer lines which, in turn, correspond to either symmetrical or asymmetrical ribbon in the longitudinal direction (see Figs. 7 and 8). A bias voltage $V_{\text{sd}} = 5.6$ eV is applied to the leads and V_{g} is set to zero. In Figs. 7 and 8, we show snapshots of the density variation and bond-current profiles. The density variation is defined as the difference between the density at time t and the ground-state density. Since the size of the ribbons is comparable to that in Sec. III A, we choose the snapshot times to correspond to the first wave crest {9,10} fs (on the left panels) and to the first wave trough {16,20} fs (on the right panels). The full density and current dynamics are shown in an animation [96].

The symmetry of the ribbon is responsible for the charge and current profiles. In the aGNR case (see Fig. 7), the top panel shows a fully symmetric 13-aGNR (invariant structure for mirrorings both in the transverse and longitudinal direction) and the bottom panel shows a 12-aGNR (invariant structure for mirroring only in the longitudinal direction). The asymmetry does not lead to dramatic differences in the charge and current distributions. In the charge profile of the symmetric aGNR, certain "cold" and "hot" spots show up in the middle region whereas in the asymmetric aGNR the charge is more evenly distributed from the source electrode to the drain electrode. Also, in both aGNR structures, the current is mostly flowing through the edges and the wavefront is flat [96]. In the zGNR case (see Fig. 8), the top panel shows an even 8-zGNR and the bottom panel shows an odd 7-zGNR. In both structures, we observe diagonal charge patterns along the ribbon; in the even zGNR these patterns are symmetric, whereas in the odd zGNR the patterns show asymmetric features. Certain cold and hot spots show up in the crossings of density wavefronts. In addition, the current is mostly flowing longitudinally through the interior of the ribbons with a much smaller contribution coming from the edges. From the animation in Ref. [96], we also see that the wavefront has a triangular shape.

The pattern of the charge-current profile is quite different at different times. On the left panels, we have a perfect wave propagating along the ribbon, whereas on the right panels we see an interference pattern due to the reflected wave. In the density-wave profile, there are two antinodes at the electrode interfaces, at the time corresponding to the first maximum ($t = 10$ fs) and one antinode together with two nodes in the

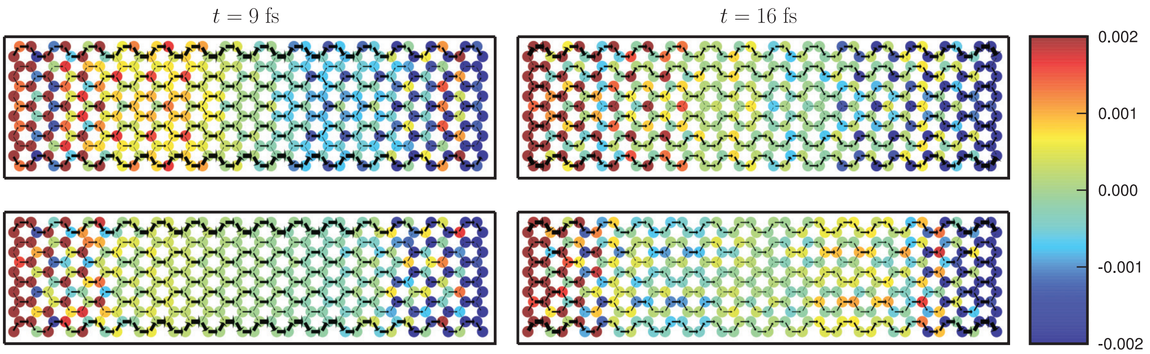

FIG. 7. (Color online) Temporal snapshots of spatial charge densities and bond currents along aGNRs. Upper panel shows the fully symmetric aGNR and lower panel transversally asymmetric aGNR. Left panel shows the snapshots corresponding to the first maximum in the transient current and the right panel shows the ones corresponding to the first minimum. The charge densities are calculated as the difference from the ground-state density (color map). The bond currents are drawn as solid arrows where the width of the arrow indicates the relative strength of the current.

middle region. At the time corresponding to the first minimum ($t = 20$ fs), the antinodes remain at the electrode interface but additional nodes arise in the middle region.

D. Perturbed central region

As an illustration of the formula in Eq. (20) for perturbed central regions, we study the transient of a 4-zGNR (or more accurately a "4 × 4 graphene flake"). The system consists of 32 carbon sites and an onsite potential ϕ_m is switched on at site m concurrently with the applied bias. Let us investigate how the form of the voltage profile within the flake affects the transient dynamics. We define x_m to be the distance of the mth carbon atom from the left interface and take $\phi_m = \phi(x_m)$. For a linear potential profile, we use

$$\phi(x_m) = -\frac{2V_\mathrm{g}}{L}x_m + V_\mathrm{g},$$

and for a sinusoidal potential profile

$$\phi(x_m) = \begin{cases} V_\mathrm{g}, & x_m < L/10 \\ V_\mathrm{g}\cos\left(\frac{5\pi}{4L}x_m - \frac{\pi}{8}\right), & L/10 \leqslant x_m \leqslant 9L/10 \\ -V_\mathrm{g}, & x_m > 9L/10 \end{cases}$$

where L is the length of the flake.

In Fig. 9, we show the time-dependent currents through the flake with fixed bias voltage $V_\mathrm{sd}/2 = 3.5$ eV and varying linear potential in panel Fig. 9(a) and sinusoidal potential in Fig. 9(b). The comparison with the previous result of nonperturbed "no gate" and perturbed "$V_\mathrm{g} = 0.0$ eV" central region provides a numerical check of the correctness of Eq. (20).

For voltages smaller than 1 eV, the transient is not so different from the nonperturbed results. However, for stronger voltages, a rather nontrivial transient behavior is observed. Notice that the largest value $V_\mathrm{g} = 3.5$ eV corresponds to the physical situation of a continuous potential profile. The Fourier spectrum of the transient is shown in Fig. 9(c). The much richer structure in several high-energy spectral windows is due to transitions involving levels of the *perturbed* central region.

The dependence of the energy and spectral weight of the levels on V_g is most clearly visualized by plotting the nonequilibrium spectral function

$$A(\omega) = -\frac{1}{\pi}\,\mathrm{Im}\,\mathrm{Tr}[G^\mathrm{R}(\omega)], \tag{23}$$

where the trace is over the states of the central region. The spectral function is displayed in Fig. 10. As expected, the spectrum widens with increasing V_g. The high-energy peaks at $\omega \approx \pm 8$ eV (in the nonperturbed case: $V_\mathrm{g} = 0$ eV) shift to $\omega \approx \pm 10$ eV (when the perturbation is at its maximum: $V_\mathrm{g} = 3.5$ eV). This is consistent with the peaks occurring at around $\omega \approx 10$ eV in Fig. 9(c). With a similar analysis, one can show that all other main peaks in the Fourier spectrum can be interpreted by inspecting the spectral function.

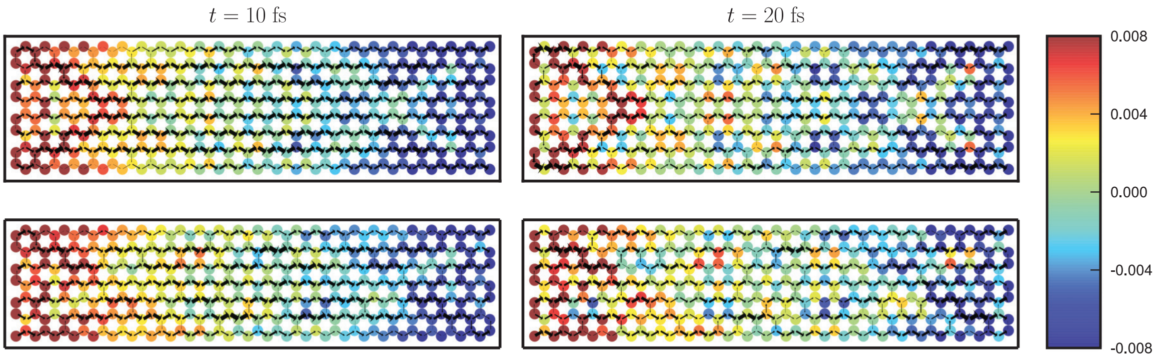

FIG. 8. (Color online) Temporal snapshots as in Fig. 7 but for zGNRs and at different times.

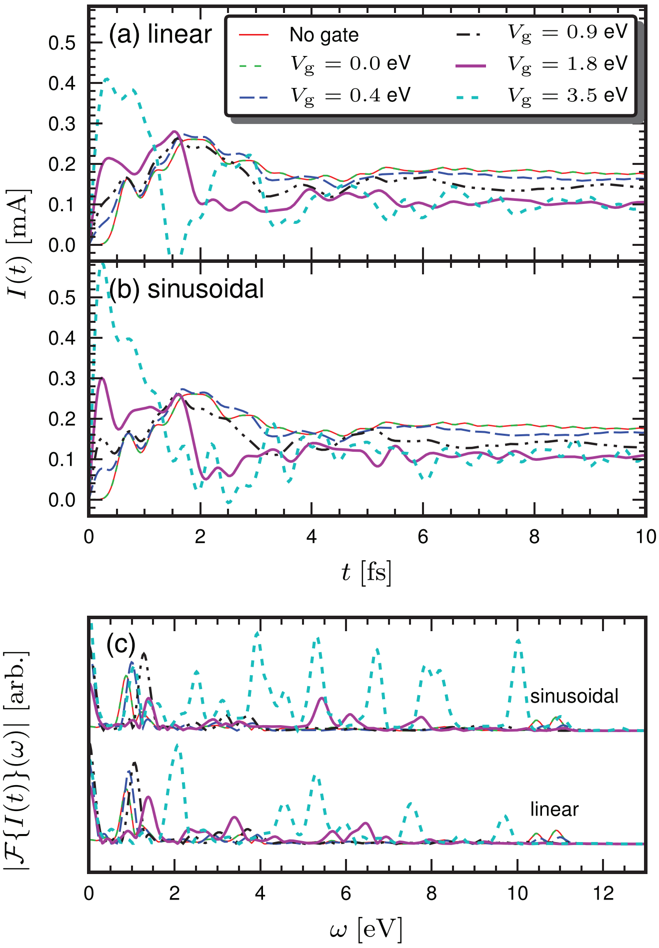

FIG. 9. (Color online) Time-dependent bond currents through a 4-zGNR (length 0.7 nm and width 0.9 nm) with fixed bias voltage $V_{\rm sd}/2 = 3.5$ eV and with *varying potentials*: (a) linear potential profile, (b) sinusoidal potential profile, (c) the corresponding Fourier transforms (sinusoidal is offset for clarity).

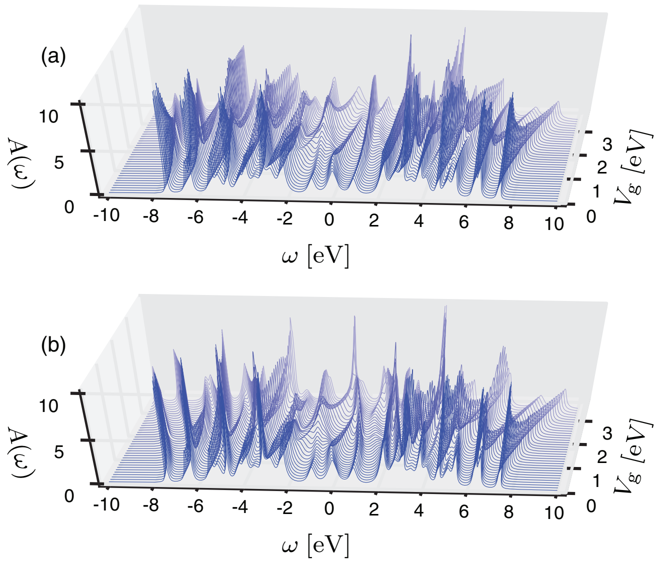

FIG. 10. (Color online) Nonequilibrium spectral functions of the studied zGNR with *varying potential*: (a) linear potential profile, and (b) sinusoidal potential profile.

IV. CONCLUSION

In this work, we developed a time-dependent extension of the Landauer-Büttiker approach to study transient dynamics in time-dependent quantum transport through molecular junctions. We have derived a closed integral expression for the time dependence of the density matrix of the molecular junction after switch-on of a bias voltage in the leads or a perturbation in the junction as well as for the current flowing into the leads. Both equations can be evaluated without the necessity of propagating individual single-particle orbitals or Green's functions. We applied the approach to study the transient dynamics of zigzag and armchair graphene nanoribbons of different symmetries. We found a rich transient dynamics in which the saturation times can exceed several hundreds of femtoseconds while displaying a long-time oscillatory motion related to multiple reflections of the density wave in the nanoribbons at the ribbon-lead interface. In the case of armchair nanoribbons, we find pronounced quasi-steady states which can be explained by multiple reflections of the density wave passing through the ribbon with the edge states located at the ribbon-lead interfaces. We see further in the case of zigzag nanoribbons that there is a predominant oscillation frequency associated with virtual transitions between the edge states and the Fermi levels of the electrode. The transient dynamics therefore gives detailed spectral information on the structure of the nanoribbons. Recently, the ultrafast dynamics of individual carbon nanotubes has been measured using laser optics by four-wave-mixing techniques [97]. There are therefore important experimental developments that can, in the future, give access to the direct study of transient dynamics. Such transient spectroscopy can give important detailed information on the structure of molecular junctions out of equilibrium.

ACKNOWLEDGMENTS

R.T. wishes to thank Väisälä Foundation of The Finnish Academy of Science and Letters for financial support and CSC, the Finnish IT Center for Science, for computing resources. R.v.L. thanks the Academy of Finland for support. E.P. and G.S. acknowledge funding by MIUR FIRB Grant No. RBFR12SW0J. G.S. acknowledges financial support through travel Grant No. Psi-K2 5813 of the European Science Foundation (ESF). C. Gomes da Rocha, A.-M. Uimonen, N. Säkkinen, and M. Hyrkäs are acknowledged for useful discussions.

APPENDIX A: RESULTS IN THE ZERO-TEMPERATURE LIMIT

By taking into account the behavior of the Fermi function in the zero-temperature limit and adjusting accordingly the integrals in Eqs. (15)–(17), we get the following explicit expressions:

$$\mathit{\Lambda}_{\alpha,jk} = \frac{\ln(\epsilon_k^* - \mu_\alpha) - \ln(\epsilon_j - \mu_\alpha)}{2\pi(\epsilon_k^* - \epsilon_j)}, \tag{A1}$$

$$\mathit{\Pi}_{\alpha,jk}(t) = \frac{e^{-i(\epsilon_j-\mu_\alpha)t}\left\{F[i(\epsilon_k^* - \mu_\alpha)t] + \frac{\epsilon_k^*-\epsilon_j-V_\alpha}{V_\alpha}F[i(\epsilon_j-\mu_\alpha)t] - \frac{\epsilon_k^*-\epsilon_j}{V_\alpha}F[i(\epsilon_j-\mu)t]\right\}}{2\pi(\epsilon_k^*-\epsilon_j)(\epsilon_k^*-\epsilon_j-V_\alpha)}, \tag{A2}$$

$$\mathit{\Omega}_{\alpha,jk} = \frac{(\epsilon_k^*-\epsilon_j+V_\alpha)[\ln(\epsilon_k^*-\mu_\alpha)-\ln(\epsilon_j-\mu)] + (\epsilon_k^*-\epsilon_j-V_\alpha)[\ln(\epsilon_j-\mu_\alpha)-\ln(\epsilon_k^*-\mu)]}{2\pi\left[(\epsilon_k^*-\epsilon_j)V_\alpha^3 - (\epsilon_k^*-\epsilon_j)^3V_\alpha\right]}, \tag{A3}$$

where we defined $\mu_\alpha = \mu + V_\alpha$ and

$$F(z) = \begin{cases} e^z[2\pi i - \mathrm{E}_1(z)], & \text{if } \arg(z) \in]-\pi,-\pi/2] \\ -e^z\mathrm{E}_1(z), & \text{otherwise.}\end{cases} \tag{A4}$$

Here ln is the principal branch complex logarithm function, arg the principal argument, and E_1 the exponential integral function:

$$\mathrm{E}_1(z) = \int_1^\infty \frac{e^{-zt}}{t}\,dt. \tag{A5}$$

About the implementation of the complex-valued (complex variable) exponential integral, there is a thorough introduction in Ref. [81]. The piecewise definition of the function F is due to branch cuts in the z plane.

We notice in Eqs. (A1)–(A3) that it is possible that the structure of the single-particle Hamiltonian h would together with the coupling matrices $\mathit{\Gamma}$ produce such an effective Hamiltonian h_{eff} with degenerate eigenvalues: $\mathrm{Im}\,\epsilon_j = 0$ and $\mathrm{Re}\,\epsilon_j = \mathrm{Re}\,\epsilon_k^*$. In this case, we consider the left/right eigenbases of the effective Hamiltonian h_{eff}: Since $h_{\text{eff}} = h_{CC} - \frac{i}{2}\mathit{\Gamma}$, where h_{CC} and $\mathit{\Gamma}$ are Hermitian matrices, then

$$\begin{aligned}\epsilon_j\langle\Psi_j^{\mathrm{L}}|\Psi_j^{\mathrm{L}}\rangle &= \langle\Psi_j^{\mathrm{L}}|h_{\text{eff}}|\Psi_j^{\mathrm{L}}\rangle \\ &= \langle\Psi_j^{\mathrm{L}}|h_{CC}|\Psi_j^{\mathrm{L}}\rangle - \frac{i}{2}\langle\Psi_j^{\mathrm{L}}|\mathit{\Gamma}|\Psi_j^{\mathrm{L}}\rangle,\end{aligned} \tag{A6}$$

which, in turn, gives

$$\epsilon_j = \frac{\langle\Psi_j^{\mathrm{L}}|h_{CC}|\Psi_j^{\mathrm{L}}\rangle}{\langle\Psi_j^{\mathrm{L}}|\Psi_j^{\mathrm{L}}\rangle} - \frac{\frac{i}{2}\langle\Psi_j^{\mathrm{L}}|\mathit{\Gamma}|\Psi_j^{\mathrm{L}}\rangle}{\langle\Psi_j^{\mathrm{L}}|\Psi_j^{\mathrm{L}}\rangle}. \tag{A7}$$

Since the expectation values are real and $\mathit{\Gamma}$ is a positive-definite matrix, we get

$$\mathrm{Im}\,\epsilon_j = -\frac{1}{2}\frac{\langle\Psi_j^{\mathrm{L}}|\mathit{\Gamma}|\Psi_j^{\mathrm{L}}\rangle}{\langle\Psi_j^{\mathrm{L}}|\Psi_j^{\mathrm{L}}\rangle} < 0. \tag{A8}$$

Then, suppose that $\mathrm{Im}\,\epsilon_j = 0$. This gives $\langle\Psi_j^{\mathrm{L}}|\mathit{\Gamma}|\Psi_j^{\mathrm{L}}\rangle = 0$, and since the level-width matrices are calculated from the tunneling matrices by $\mathit{\Gamma} \sim T^\dagger T$, we get

$$\langle\Psi_j^{\mathrm{L}}|T^\dagger T|\Psi_j^{\mathrm{L}}\rangle = 0 \;\Rightarrow\; \langle\chi_j^{\mathrm{L}}|\chi_j^{\mathrm{L}}\rangle = 0, \tag{A9}$$

where $|\chi_j^{\mathrm{L}}\rangle = T|\Psi_j^{\mathrm{L}}\rangle$. Having then a zero-norm vector $|\chi_j^{\mathrm{L}}\rangle$ it means that vector itself must be zero, i.e., $0 = |\chi_j^{\mathrm{L}}\rangle = T|\Psi_j^{\mathrm{L}}\rangle$ for all j. This means that $|\Psi_j^{\mathrm{L}}\rangle$ is an eigenvector of T with zero eigenvalue. In particular, $\mathit{\Gamma}|\Psi_j^{\mathrm{L}}\rangle = T^\dagger T|\Psi_j^{\mathrm{L}}\rangle = 0$, and hence

$$\mathit{\Gamma}_{jk} = \langle\Psi_j^{\mathrm{L}}|\mathit{\Gamma}|\Psi_k^{\mathrm{L}}\rangle = 0,\ \forall\ j,k. \tag{A10}$$

Therefore, the case of degenerate eigenvalues can be excluded from the derived formulas altogether. This also relates to some particular systems having states that are eigenfunctions of $\mathit{\Gamma}_{\alpha,mn}$ with zero eigenvalue. In these cases, it becomes important to take into account the infinitesimal $i\eta$ in the retarded Green's function for these states, i.e., the Green's function operator acting on these states has the effective form $G^{\mathrm{R}}(\omega) = (\omega - h_{CC} + i\eta)^{-1}$. This effectively amounts to an infinitesimal value of $\mathit{\Gamma}_{\alpha,mn}$ for these particular states in Eq. (13) which leads to sharp delta peaks in the spectral function. However, since these states are inert and do not contribute to the dynamics, they only affect the static part of the density matrix. Numerically, it is then more advantageous to calculate these states separately and add a cutoff in Eq. (13). We evaluate Eq. (13) only for $\mathit{\Gamma}_{\alpha,mn} > \epsilon$ with ϵ a small number and treat the inert states separately. The part of the density matrix corresponding to these inert states is then given by

$$\hat{\rho} = \sum_{\epsilon_j<\mu} |\phi_j\rangle\langle\phi_j|, \tag{A11}$$

where we sum over all eigenstates of h_{CC} that satisfy $\mathit{\Gamma}_\alpha|\phi_j\rangle = 0$ for all α. Note that the existence of the inert states is a very special case caused by symmetries of the molecule and $\mathit{\Gamma}_\alpha$. The only case we encountered in this study where such states exist is the case of the fully symmetric aGNR of Fig. 7. There, the inert states are given by wave functions that have nodal planes exactly at the rows which are contacted to the leads.

APPENDIX B: RESULTS FOR THE PERTURBED CENTRAL REGION

In this appendix, we guide the reader through the derivation of Eq. (20). As we will often refer to results in Ref. [73], we here append the suffix "I" to every equation or section in this reference. The results of Ref. [73] are general and remain valid in the presence of electric or magnetic fields in the central region until Sec. 3.2-I. In the Green's function calculations, the Matsubara Green's function does not change as it depends only on the ground-state Hamiltonian h_{CC}. On the other hand, for Green's functions having components on the horizontal branch of the Keldysh contour, we have to use the Hamiltonian $\widetilde{h}_{CC}$. Therefore, the Eqs. (24-I) and (25-I) change according to

$$G^{\rceil}(t,\tau) = e^{-i\widetilde{h}_{\text{eff}}t}\left[G^{\text{M}}(0,\tau) - \int_0^t dt' e^{i\widetilde{h}_{\text{eff}}t'} \times \int_0^\beta d\bar{\tau}\, \Sigma^{\rceil}(t',\bar{\tau})G^{\text{M}}(\bar{\tau},\tau)\right], \tag{B1}$$

$$G^{\text{R}}(t-t') = -i\theta(t-t')e^{-i\widetilde{h}_{\text{eff}}(t-t')}, \tag{B2}$$

where $\widetilde{h}_{\text{eff}} = \widetilde{h}_{CC} - \frac{i}{2}\Gamma$. All steps in Appendix C-I and D-I as well as in Sec. 3.3-I should change accordingly. In particular, we stress the G^{M} and G^{R} in Eq. (C.9-I) are now different, that $\widetilde{V}_\alpha$ is a matrix (Appendix D-I) and that the Dyson-type equation [Eq. (D.1-I)] relating the nonperturbed and perturbed Green's functions now reads as

$$G^{\text{R}}(\omega) - \widetilde{G}^{\text{R}}(\omega + V_\alpha) = G^{\text{R}}(\omega)\widetilde{V}_\alpha \widetilde{G}^{\text{R}}(\omega + V_\alpha). \tag{B3}$$

With these considerations and following the same steps as in Ref. [73], we arrive at the result shown in Eq. (20).

Next, by expanding in the *left* eigenbasis of $\widetilde{h}_{\text{eff}}$ we find

$$\begin{aligned}\widetilde{\rho}_{jk}(t) &= \langle \widetilde{\Psi}_j^{\text{L}} | \rho(t) | \widetilde{\Psi}_k^{\text{L}} \rangle \\ &= \sum_\alpha [\widetilde{\Gamma}_{\alpha,jk}\widetilde{\Lambda}_{\alpha,jk} + \widetilde{\Pi}_{\alpha,jk}(t) + \widetilde{\Pi}^*_{\alpha,kj}(t) + \widetilde{\Omega}_{\alpha,jk}(t)]\end{aligned} \tag{B4}$$

with the introduced functions

$$\begin{aligned}
\widetilde{\Gamma}_{\alpha,jk} &= \langle \widetilde{\Psi}_j^{\text{L}} | \Gamma_\alpha | \widetilde{\Psi}_k^{\text{L}} \rangle, \\
\widetilde{\Lambda}_{\alpha,jk} &= \int \frac{d\omega}{2\pi} \frac{f(\omega-\mu)}{(\omega + V_\alpha - \widetilde{\epsilon}_j)(\omega + V_\alpha - \widetilde{\epsilon}_k^*)}, \\
\widetilde{\Pi}_{\alpha,jk}(t) &= \sum_{m,n} \frac{\langle \widetilde{\Psi}_j^{\text{L}} | \Psi_m^{\text{R}} \rangle \langle \Psi_m^{\text{L}} | \widetilde{V}_\alpha | \widetilde{\Psi}_n^{\text{R}} \rangle \widetilde{\Gamma}_{\alpha,nk}}{\langle \Psi_m^{\text{L}} | \Psi_m^{\text{R}} \rangle \langle \widetilde{\Psi}_n^{\text{L}} | \widetilde{\Psi}_n^{\text{R}} \rangle} \int \frac{d\omega}{2\pi} \frac{f(\omega-\mu)e^{i(\omega + V_\alpha - \widetilde{\epsilon}_j)t}}{(\omega - \epsilon_m)(\omega + V_\alpha - \widetilde{\epsilon}_n)(\omega + V_\alpha - \widetilde{\epsilon}_k^*)}, \\
\widetilde{\Omega}_{\alpha,jk}(t) &= \sum_{m,n,p,q} \frac{\langle \widetilde{\Psi}_j^{\text{L}} | \Psi_m^{\text{R}} \rangle \langle \Psi_m^{\text{L}} | \widetilde{V}_\alpha | \widetilde{\Psi}_n^{\text{R}} \rangle \widetilde{\Gamma}_{\alpha,np} \langle \widetilde{\Psi}_p^{\text{R}} | \widetilde{V}_\alpha^\dagger | \Psi_q^{\text{L}} \rangle \langle \Psi_q^{\text{R}} | \widetilde{\Psi}_k^{\text{L}} \rangle}{\langle \Psi_m^{\text{L}} | \Psi_m^{\text{R}} \rangle \langle \widetilde{\Psi}_n^{\text{L}} | \widetilde{\Psi}_n^{\text{R}} \rangle \langle \widetilde{\Psi}_p^{\text{R}} | \widetilde{\Psi}_p^{\text{L}} \rangle \langle \Psi_q^{\text{R}} | \Psi_q^{\text{L}} \rangle} \\
&\quad \times e^{-i(\widetilde{\epsilon}_j - \widetilde{\epsilon}_k^*)t} \int \frac{d\omega}{2\pi} \frac{f(\omega-\mu)}{(\omega - \epsilon_m)(\omega + V_\alpha - \widetilde{\epsilon}_n)(\omega + V_\alpha - \widetilde{\epsilon}_p^*)(\omega - \epsilon_q^*)},
\end{aligned} \tag{B5}$$

where eigenvalues ϵ_j and $\widetilde{\epsilon}_k^*$ refer to the complex eigenvalues of h_{eff} and $\widetilde{h}_{\text{eff}}$, respectively. In the limit $\widetilde{h}_{\text{eff}} \to h_{\text{eff}}$, this result can also be checked to reduce to the earlier result in Eqs. (13), (15), (16), and (17). In the limit of uncontacted system, Eq. (B4) describes the dynamics of an isolated (perturbed) system, in which case the same result could be derived directly from the equations of motion of the one-particle density matrix.

In the zero-temperature limit, the integrals in Eq. (B5) can be calculated analytically also in this case. The integrals now only have more constants and the final results can not be simplified as much as earlier. The explicit forms can be found in the following:

$$\widetilde{\Lambda}_{\alpha,jk} = \frac{\ln(\widetilde{\epsilon}_k^* - \mu_\alpha) - \ln(\widetilde{\epsilon}_j - \mu_\alpha)}{2\pi(\widetilde{\epsilon}_k^* - \widetilde{\epsilon}_j)}, \tag{B6}$$

$$\begin{aligned}
\widetilde{\Pi}_{\alpha,jk}(t) &= \sum_{m,n} \frac{\langle \widetilde{\Psi}_j^{\text{L}} | \Psi_m^{\text{R}} \rangle \langle \Psi_m^{\text{L}} | \widetilde{V}_\alpha | \widetilde{\Psi}_n^{\text{R}} \rangle \langle \widetilde{\Psi}_n^{\text{L}} | \Gamma_\alpha | \widetilde{\Psi}_k^{\text{L}} \rangle}{\langle \Psi_m^{\text{L}} | \Psi_m^{\text{R}} \rangle \langle \widetilde{\Psi}_n^{\text{L}} | \widetilde{\Psi}_n^{\text{R}} \rangle} \frac{e^{-i(\widetilde{\epsilon}_j - \mu_\alpha)t}}{2\pi(\widetilde{\epsilon}_k^* - \widetilde{\epsilon}_n)(\widetilde{\epsilon}_k^* - \epsilon_m - V_\alpha)} \\
&\quad \times \left\{ F[i(\widetilde{\epsilon}_k^* - \mu_\alpha)t] - \frac{\widetilde{\epsilon}_k^* - \epsilon_m - V_\alpha}{\widetilde{\epsilon}_n - \epsilon_m - V_\alpha} F[i(\widetilde{\epsilon}_n - \mu_\alpha)t] + \frac{\widetilde{\epsilon}_k^* - \widetilde{\epsilon}_n}{\widetilde{\epsilon}_n - \epsilon_m - V_\alpha} F[i(\epsilon_m - \mu)t] \right\},
\end{aligned} \tag{B7}$$

$$\begin{aligned}
\widetilde{\Omega}_{\alpha,jk}(t) &= \sum_{m,n,p,q} \frac{\langle \widetilde{\Psi}_j^{\text{L}} | \Psi_m^{\text{R}} \rangle \langle \Psi_m^{\text{L}} | \widetilde{V}_\alpha | \widetilde{\Psi}_n^{\text{R}} \rangle \langle \widetilde{\Psi}_n^{\text{L}} | \Gamma_\alpha | \widetilde{\Psi}_p^{\text{L}} \rangle \langle \widetilde{\Psi}_p^{\text{R}} | \widetilde{V}_\alpha^\dagger | \Psi_q^{\text{L}} \rangle \langle \Psi_q^{\text{R}} | \widetilde{\Psi}_k^{\text{L}} \rangle}{\langle \Psi_m^{\text{L}} | \Psi_m^{\text{R}} \rangle \langle \widetilde{\Psi}_n^{\text{L}} | \widetilde{\Psi}_n^{\text{R}} \rangle \langle \widetilde{\Psi}_p^{\text{R}} | \widetilde{\Psi}_p^{\text{L}} \rangle \langle \Psi_q^{\text{R}} | \Psi_q^{\text{L}} \rangle} \frac{e^{-i(\widetilde{\epsilon}_j - \widetilde{\epsilon}_k^*)t}}{2\pi} \\
&\quad \times \left[\frac{\ln(\epsilon_m - \mu)}{(\epsilon_m - \widetilde{\epsilon}_n + V_\alpha)(\epsilon_m - \widetilde{\epsilon}_p^* + V_\alpha)(\epsilon_m - \epsilon_q^*)} + \frac{\ln(\widetilde{\epsilon}_n - \mu_\alpha)}{(\widetilde{\epsilon}_n - \epsilon_m - V_\alpha)(\widetilde{\epsilon}_n - \widetilde{\epsilon}_p^*)(\widetilde{\epsilon}_n - \epsilon_q^* - V_\alpha)} \right. \\
&\quad \left. + \frac{\ln(\epsilon_q^* - \mu)}{(\epsilon_q^* - \epsilon_m)(\epsilon_q^* - \widetilde{\epsilon}_n + V_\alpha)(\epsilon_q^* - \widetilde{\epsilon}_p^* + V_\alpha)} + \frac{\ln(\widetilde{\epsilon}_p^* - \mu_\alpha)}{(\widetilde{\epsilon}_p^* - \epsilon_m - V_\alpha)(\widetilde{\epsilon}_p^* - \widetilde{\epsilon}_n)(\widetilde{\epsilon}_p^* - \epsilon_q^* - V_\alpha)} \right],
\end{aligned} \tag{B8}$$

where $\mu_\alpha = \mu + V_\alpha$ and F is as in Eq. (A4). Also, these results can be checked to reduce to the earlier results in Eqs. (A1)–(A3) when $\widetilde{\Psi} \to \Psi$ and $\widetilde{\epsilon} \to \epsilon$ ($\widetilde{h}_{\text{eff}} \to h_{\text{eff}}$).

[1] R. Landauer, IBM J. Res. Dev. **1**, 223 (1957).
[2] M. Büttiker, Phys. Rev. Lett. **57**, 1761 (1986).
[3] N. D. Lang, Phys. Rev. B **52**, 5335 (1995).
[4] N. D. Lang and P. Avouris, Phys. Rev. Lett. **81**, 3515 (1998).
[5] J. Taylor, H. Guo, and J. Wang, Phys. Rev. B **63**, 121104 (2001).
[6] J. Taylor and H. Guo, Phys. Rev. B **63**, 245407 (2001).
[7] M. Brandbyge, J. L. Mozos, P. Ordejon, J. Taylor, and K. Stokbro, Phys. Rev. B **65**, 165401 (2002).
[8] G. Stefanucci and C.-O. Almbladh, Europhys. Lett. **67**, 14 (2004).
[9] F. Evers, F. Weigend, and M. Koentopp, Phys. Rev. B **69**, 235411 (2004).
[10] S. Kurth, G. Stefanucci, C.-O. Almbladh, A. Rubio, and E. K. U. Gross, Phys. Rev. B **72**, 035308 (2005).
[11] X. Qian, J. Li, X. Lin, and S. Yip, Phys. Rev. B **73**, 035408 (2006).
[12] G. Stefanucci, E. Perfetto, and M. Cini, Phys. Rev. B **78**, 075425 (2008).
[13] Z. Zhou and S.-I. Chu, Europhys. Lett. **88**, 17008 (2009).
[14] G. Stefanucci, E. Perfetto, and M. Cini, Phys. Rev. B **81**, 115446 (2010).
[15] B. Gaury *et al.*, Phys. Rep. **534**, 1 (2014).
[16] P. Bokes, F. Corsetti, and R. W. Godby, Phys. Rev. Lett. **101**, 046402 (2008).
[17] A. Chaves, G. A. Farias, F. M. Peeters, and B. Szafran, Phys. Rev. B **80**, 125331 (2009).
[18] P. Bokes, Phys. Rev. A **83**, 032104 (2011).
[19] N. Bushong, N. Sai, and M. D. Ventra, Nano Lett **5**, 2569 (2005).
[20] C.-L. Cheng, J. S. Evans, and T. V. Voorhis, Phys. Rev. B **74**, 155112 (2006).
[21] N. Sai, N. Bushong, R. Hatcher, and M. DiVentra, Phys. Rev. B **75**, 115410 (2007).
[22] H. Eshuis and T. van Voorhis, Chem. Phys. Phys. Chem. **11**, 10293 (2009).
[23] R. Baer, T. Seideman, S. Ilani, and D. Neuhauser, J. Chem. Phys. **120**, 3387 (2004).
[24] K. Varga, Phys. Rev. B **83**, 195130 (2011).
[25] L. Zhang, J. Chen, and J. Wang, Phys. Rev. B **87**, 205401 (2013).
[26] J. Maciejko, J. Wang, and H. Guo, Phys. Rev. B **74**, 085324 (2006).
[27] X.-Q. Li and Y. J. Yan, Phys. Rev. B **75**, 075114 (2007).
[28] V. Moldoveanu, V. Gudmundsson, and A. Manolescu, Phys. Rev. B **76**, 085330 (2007).
[29] A. Prociuk and B. D. Dunietz, Phys. Rev. B **78**, 165112 (2008).
[30] A. Croy and U. Saalmann, Phys. Rev. B **80**, 245311 (2009).
[31] X. Zheng *et al.*, J. Chem. Phys. **133**, 114101 (2010).
[32] Y. Xing, B. Wang, and J. Wang, Phys. Rev. B **82**, 205112 (2010).
[33] H. Xie *et al.*, J. Chem Phys. **137**, 044113 (2012).
[34] L. Zhang, Y. Xing, and J. Wang, Phys. Rev. B **86**, 155438 (2012).
[35] A. Pertsova, M. Stamenova, and S. Sanvito, J. Phys.: Condens. Matter **25**, 105501 (2013).
[36] Y. Zhang, S. Chen, and G. H. Chen, Phys. Rev. B **87**, 085110 (2013).
[37] E. McEniry *et al.*, J. Phys.: Condens. Matter **19**, 196201 (2007).
[38] P. Myöhänen, A. Stan, G. Stefanucci, and R. van Leeuwen, Europhys. Lett. **84**, 67001 (2008).
[39] P. Myöhänen, A. Stan, G. Stefanucci, and R. van Leeuwen, Phys. Rev. B **80**, 115107 (2009).
[40] M. Puig von Friesen, C. Verdozzi, and C.-O. Almbladh, Phys. Rev. B **82**, 155108 (2010).
[41] J. N. Pedersen and A. Wacker, Phys. Rev. B **72**, 195330 (2005).
[42] S. Welack, M. Schreiber, and U. Kleinekathöfer, J. Chem. Phys. **124**, 044712 (2006).
[43] H. Wang and M. Thoss, J. Chem. Phys. **131**, 024114 (2009).
[44] V. Moldoveanu, V. Gudmundsson, and A. Manolescu, New J. Phys. **11**, 073019 (2009).
[45] P. Zedler, G. Schaller, G. Kiesslich, C. Emary, and T. Brandes, Phys. Rev. B **80**, 045309 (2009).
[46] J. N. Pedersen and A. Wacker, Phys. E (Amsterdam) **42**, 595 (2010).
[47] S. Wang, X. Zheng, J. Jin, and Y. J. Yan, Phys. Rev. B **88**, 035129 (2013).
[48] S. Weiss, J. Eckel, M. Thorwart, and R. Egger, Phys. Rev. B **77**, 195316 (2008).
[49] M. Schiro and M. Fabrizio, Phys. Rev. B **79**, 153302 (2009).
[50] D. Segal, A. J. Millis, and D. R. Reichman, Phys. Rev. B **82**, 205323 (2010).
[51] G. Cohen and E. Rabani, Phys. Rev. B **84**, 075150 (2011).
[52] F. B. Anders and A. Schiller, Phys. Rev. Lett. **95**, 196801 (2005).
[53] F. B. Anders and A. Schiller, Phys. Rev. B **74**, 245113 (2006).
[54] M. Pletyukhov, D. Schuricht, and H. Schoeller, Phys. Rev. Lett. **104**, 106801 (2010).
[55] P. Wang and S. Kehrein, Phys. Rev. B **82**, 125124 (2010).
[56] S. Andergassen, M. Pletyukhov, D. Schuricht, H. Schoeller, and L. Borda, Phys. Rev. B **83**, 205103 (2011).
[57] D. M. Kennes, S. G. Jakobs, C. Karrasch, and V. Meden, Phys. Rev. B **85**, 085113 (2012).
[58] E. Eidelstein, A. Schiller, F. Guttge, and F. B. Anders, Phys. Rev. B **85**, 075118 (2012).
[59] X. Oriols, Phys. Rev. Lett. **98**, 066803 (2007).
[60] G. Albareda, J. Sune, and X. Oriols, Phys. Rev. B **79**, 075315 (2009).
[61] G. Vidal, Phys. Rev. Lett. **93**, 040502 (2004).
[62] P. Schmitteckert, Phys. Rev. B **70**, 121302 (2004).
[63] S. R. White and A. E. Feiguin, Phys. Rev. Lett. **93**, 076401 (2004).
[64] A. Branschädel, G. Schneider, and P. Schmitteckert, Ann. Phys. (Berlin) **522**, 657 (2010).
[65] U. Schollwöck, Ann. Phys. (NY) **326**, 96 (2011).
[66] P. Werner, T. Oka, and A. J. Millis, Phys. Rev. B **79**, 035320 (2009).
[67] P. Werner, T. Oka, M. Eckstein, and A. J. Millis, Phys. Rev. B **81**, 035108 (2010).
[68] See, for instance, J. C. Cuevas and E. Scheer, *Molecular Electronics: An Introduction to Theory and Experiments* (World Scientific, Singapore, 2010).
[69] A.-P. Jauho, N. S. Wingreen, and Y. Meir, Phys. Rev. B **50**, 5528 (1994).
[70] G. Stefanucci and C.-O. Almbladh, Phys. Rev. B **69**, 195318 (2004).
[71] E. Perfetto, G. Stefanucci, and M. Cini, Phys. Rev. B **78**, 155301 (2008).
[72] G. Stefanucci and R. van Leeuwen, *Nonequilibrium Many-Body Theory of Quantum Systems: A Modern Introduction* (Cambridge University Press, Cambridge, UK, 2013).
[73] R. Tuovinen, R. van Leeuwen, E. Perfetto, and G. Stefanucci, J. Phys.: Conf. Ser. **427**, 012014 (2013).
[74] A. H. C. Neto, F. Guinea, N. M. R. Peres, K. S. Novoselov, and A. K. Geim, Rev. Mod. Phys. **81**, 109 (2009).

[75] M. I. Katsnelson, *Graphene: Carbon in Two Dimensions* (Cambridge University Press, Cambridge, UK, 2012).

[76] A. Onipko, Phys. Rev. B **78**, 245412 (2008).

[77] K. Wakabayashi, K. Sasaki, T. Nakanishi, and T. Enoki, Sci. Tech. Adv. Mater. **11**, 054504 (2010).

[78] H. Xie *et al.*, Phys. Status Solidi B **250**, 2481 (2013).

[79] E. Perfetto, G. Stefanucci, and M. Cini, Phys. Rev. B **82**, 035446 (2010).

[80] L. P. Kadanoff and G. Baym, *Quantum Statistical Mechanics* (Benjamin, New York, 1962).

[81] V. Pegoraro and P. Slusallek, J. Graphics, GPU Game Tools **15**, 183 (2011).

[82] I. V. Tokatly, Phys. Rev. B **83**, 035127 (2011).

[83] Y. Hancock, A. Uppstu, K. Saloriutta, A. Harju, and M. J. Puska, Phys. Rev. B **81**, 245402 (2010).

[84] H. Schomerus, Phys. Rev. B **76**, 045433 (2007).

[85] Y. M. Blanter and I. Martin, Phys. Rev. B **76**, 155433 (2007).

[86] K. Wakabayashi, Y. Takane, M. Yamamoto, and M. Sigrist, New J. Phys. **11**, 095016 (2009).

[87] R. B. Blackman and J. W. Tukey, *Particular Pairs of Windows: In The Measurement of Power Spectra, From the Point of View of Communications Engineering* (Dover, New York, 1959), pp. 98–99.

[88] X. Wang, Y. Ouyang, X. Li, H. Wang, J. Guo, and H. Dai, Phys. Rev. Lett. **100**, 206803 (2008).

[89] M.-W. Lin *et al.*, Nanotechnology **22**, 265201 (2011).

[90] X. Li, X. Wang, L. Zhang, S. Lee, and H. Dai, Science **319**, 1229 (2008).

[91] Y. Lu, C. A. Merchant, M. Drndić, and A. T. C. Johnson, Nano Letters **11**, 5184 (2011).

[92] Q. Yan *et al.*, Nano Lett. **7**, 1469 (2007).

[93] G. Liang *et al.*, IEEE Trans. Electron Dev. **54**, 677 (2007).

[94] I. Meric *et al.*, Nat. Nanotechnol. **3**, 654 (2008).

[95] Z. Li, H. Qian, J. Wu, B.-L. Gu, and W. Duan, Phys. Rev. Lett. **100**, 206802 (2008).

[96] See Supplemental Material at http://link.aps.org/supplemental/10.1103/PhysRevB.89.085131 for the animations corresponding to Figs. 7 and 8.

[97] P. Myllyperkiö *et al.*, ACS Nano **4**, 6780 (2010).